Steady-state Analysis of Supersonic Mixing Enhanced by a Three-dimensional Cavity Flow

Takayuki Oka[1,*], Taro Handa[2], Fujio Akagi[3], Sumio Yamaguchi[3], Toshiyuki Aoki[1], Koichiro Yamabe[1], Yusuke Kihara[1]

[1]Department of Energy and Environmental Engineering
Interdisciplinary Graduate School of Engineering Sciences, Kyushu University
6-1 Kasuga-Koen, Kasuga, Fukuoka 816-8580 Japan
[2]Department of Advanced Science and Technology, Toyota Technological Institute
2-12-1 Hisakata, Tempaku-Ku, Nagoya, Aichi 468-8511 Japan
[3]Department of Mechanical Engineering, Fukuoka University
8-19-1 Nanakuma, Jyounan-Ku, Fukuoka 814-0180 Japan

*Author to whom correspondence should be addressed,
E-mail: takayuki.oka@kyudai.jp

(Received February 7, 2017; accepted March 1, 2017).

The supersonic mixing field induced by a novel wall-mounted cavity having a three-dimensional shape is investigated computationally. In the computation, the Reynolds-averaged Navier-Stokes (RANS) equations are solved to obtain the steady state solution. The resulting pattern of limiting streamlines is compared with the previous result of oil-flow surface visualization. The comparison shows that the pattern of limiting streamlines agrees well with the oil flow pattern not only inside the cavity but also around the injector. The computational jet-penetration heights are also compared with the experimental heights measured previously. The comparison shows that both heights agree well near the injector. Such agreements imply that the flows in the cavity and around the injector can be reproduced well by the present numerical simulation. The detailed flow structure is investigated using the computational results. It is found from the results that a vortex having a three-dimensional shape is produced in the cavity and that the shear-layer spanning the cavity deflects upward near the central plane of the duct owing to the upward flows induced by the vortex. It is also found that owing to the upward shear-layer deflection the jet discharged from the injector is protected from the primary flow having large momentum. As a result, the jet penetrates highly into the primary flow.

Keywords: Supersonic flow, Cavity flow, Mixing enhancement, Numerical simulation, Jet.

1. Introduction

Supersonic mixing is one of the most important issues for the development of the scramjet engine[1)]. This application has a necessity to make the injectant mix into the primary flow for a short distance although a supersonic shear layer is more stable than a subsonic shear layer; i.e., the growth rate of the shear layer decreases with an increase in the convective Mach number. Owing to such a feature of the supersonic shear layer, it is difficult to mix the injectant rapidly into a supersonic primary flow. The rapid mixing leads us to improve the energy conversion efficiency, which means that the rapid mixing is one of the methods to assist effective utilization of energy resources and to solve the problem of lack of energy resources[2)3)].

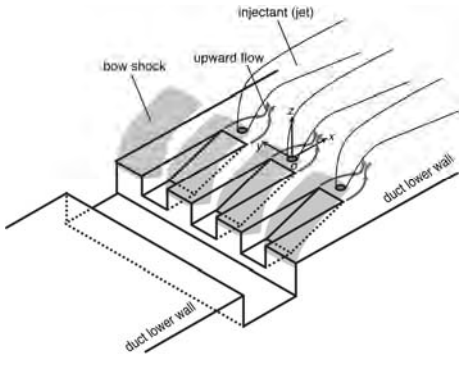

Fig. 1: New device for enhancing supersonic mixing[16)].

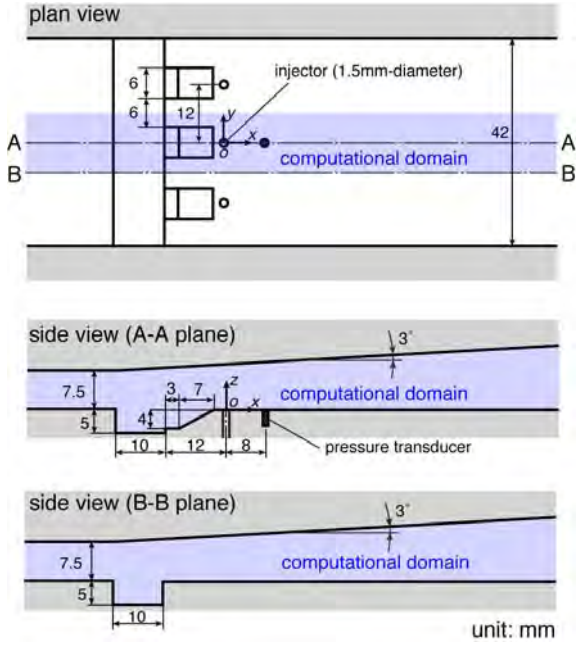

Fig. 2: Duct with the new device[16)]

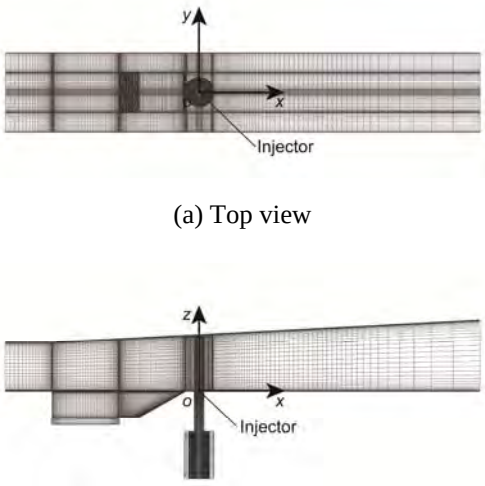

(a) Top view

(b) Side view

Fig. 3: Computational grids.

Table 1: Test conditions[16)].

freestream Mach number (air)	1.58
freestream stagnation pressure	101 kPa
freestream stagnation temperature	291 K
stagnation pressure of injectant (nitrogen)	169 kPa
stagnation temperature of injectant	291 K

A lot of techniques have been proposed for enhancing supersonic mixing; e.g., enhancement using a ramp injector[4)], lobed strut[5)], pylon[6)], elliptical injector[7)], diamond shaped orifice[8)], shallow-tail cavity[9)], wavy-wall[10)], fin-guided fuel injection[11)], wall mounted cavity[12)13)14)], a multi-sided wheel within the injector[15)], and so on.

Recently, one of the authors proposed a novel wall-mounted cavity having a three-dimensional shape as shown in Fig. 1[16)]. This cavity induces not only secondary flows but also pressure disturbances, both of which are advantageous in supersonic mixing and cannot be induced in any other previous devices. They also demonstrated experimentally the performance of the proposed device. They visualized the injectant (supersonic jet) using a planar laser-induced fluorescence (PLIF) technique. It was found from the visualization results that the jet is penetrated more highly into the primary flow using the proposed device than using a conventional device (rectangular cavity); i.e., the jet for the proposed device became up to 1.3 times as high as that for the conventional device[16)].

The jet penetration height is considered to be one of the criterions for supersonic mixing enhancement, and so the mechanism by which the jet is penetrated highly into the primary flow by the proposed device should be clarified. However, the mechanism remains unclear owing to lack of experimental information. In the present study, the three-dimensional flow structure is investigated by performing the numerical simulation in which the Reynolds-averaged Navier-Stokes (RANS) equations with a turbulence model are solved.

2. Computed flow

In the present study, the flow created in the duct shown in Fig. 2 is computed. The proposed device[16)] is mounted in the duct. A contoured symmetric nozzle, which creates a uniform supersonic aerial flow at its exit, is connected to the duct. The height and width of the duct at its entrance are 7.5 mm and 42 mm, respectively. The duct has a section with a 3° divergence angle in order to avoid unstarting in the wind tunnel due to injection or boundary-layer growth.

The cavity is mounted so that its leading edge is placed at the entrance of the divergent section. Three parts of the rear face of the rectangular cavity are cut out as shown in Fig. 2. The cut out part has a sloped wall whose angle is 30° (see side view of A-A plane). The length and depth of the cavity are 10 mm and 5 mm, respectively (see side view of B-B plane). The length and width of a cut out part are 10 mm and 6 mm, respectively. The injection ports of d = 1.5 mm diameter are located 22 mm downstream from the entrance of the divergence section. In the experiments[16)], nitrogen gas was injected

transversely into the primary flow. The coordinate system used to analyze the results is shown in Fig. 2, where *x*, *y*, and *z* indicate the streamwise, spanwise, and height coordinates, respectively.

The test conditions are summarized in Table 1. The values in the table were measured by Handa et al.[16] The free-stream Reynolds number calculated based on the variables at the entrance of the divergent section is 1.12×10^5. The momentum flux ratio is estimated to be 1.5 from the stagnation pressure and temperature of injectant.

3. Numerical analysis

The steady state computation was conducted using the commercial software Fluent 14.0. The governing equations are the three-dimensional compressible Reynolds-averaged Navier-Stokes equations. The eddy viscosity was estimated with the k-ω SST turbulence model[17]. The inviscid flux was estimated by the ASUM+ scheme based on the low Mach preconditioning method[18]. The equations were discretized in space using the finite volume method and in time using the first-order implicit method. The upwind difference scheme based on the MUSCL interpolation was applied to evaluate the convection terms. This scheme has third-order accuracy in space.

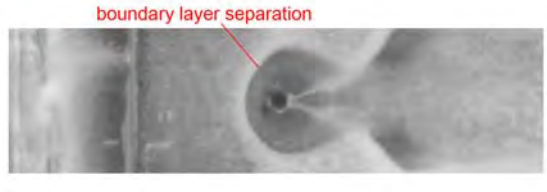

(a) duct with a rectangle cavity

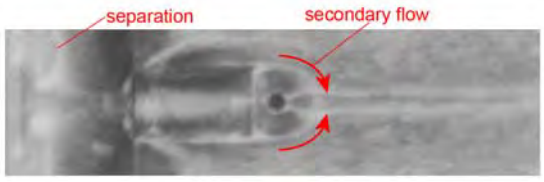

(b) duct with a three-dimensional cavity

Fig. 4: Oil flow visualization[16].

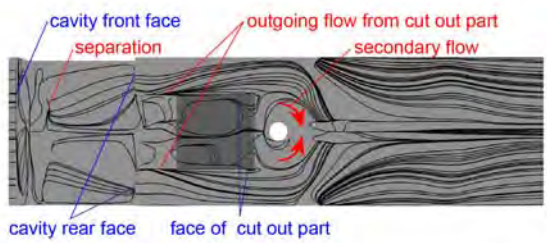

Fig. 5: Limiting streamlines on the duct lower wall.

In this study, the numerical simulation was carried out in the limited domain shown by blue color in Fig. 2 because the oil flow surface visualization revealed that the flow structure was periodic along the spanwise direction (y direction); i.e., the domain corresponds to a period of the periodicity. Although the side-wall of the duct have an influence on the flows, the regions where the flows are influenced are limited to close to the walls. As mentioned in the following chapter, we validate the computational results by comparing the computational flow with the experimental flow in the limited region including the middle injector because the flow in the region is not influenced by the duct side-wall. The computational grids used in the present simulation are shown in Fig. 3. The minimum grid spacing is less than 4.0×10^{-6} m ($y+ < 1$) on the duct walls. The total number of cells is approximately 1.69×10^6. We checked the dependence of the solution on the number of grid points by calculating the flow with 3.07×10^6. No discernible difference was observed between these two results. The inlet condition was determined by a preliminary calculation of the flow upstream from the inlet boundary; i.e., the simulation was performed in the nozzle region. At the outlet boundary, the static pressure was set to 7 kPa so that the flow became underexpanded everywhere in the duct. The no-slip boundary condition was applied on the duct wall. At the boundary facing to a side-wall of the duct, the periodic boundary condition was applied.

4. Results and discussion

Figure 4 shows the results of the oil-flow visualizations. The images in the figure are the same as those shown in the previous literature[16]. However, a displayed region is extended so that the pattern inside the cavity is seen but the region is limited so that the oil-flow pattern is easily compared with the computational result; i.e., the region corresponding to a period of periodicity is shown. Figure 4(a) shows that the oil-flow pattern on the wall of the duct with a rectangular cavity. The shape of the cavity is the same as that of the three-dimensional cavity (proposed device) except the cut out parts. In Fig 4(a), oil streak lines resulting from boundary-layer separation are observed upstream from the injection port. This boundary-layer separation is caused by the adverse pressure gradient across the bow shock wave formed in front of the jet issuing from the injector. Such a bow shock wave was observed in many previous studies[19][20]. The oil-flow pattern for the duct with the proposed device (Fig. 4(b)) is quite different from that for the duct with the rectangular cavity (Fig. 4(a)). The pattern shown in Fig. 4(b) shows evidence that the proposed device produces secondary flows moving around a jet. It is clear from the figure that the two secondary flows coming from both sides of the jet collide with each other behind the jet. Figure 5 shows the computed limiting streamlines. The pattern of the secondary flows around the jet,

outgoing flows from the cut out part into the duct, and separation line inside the cavity in the computational results (Fig. 5) are very similar to those in the oil flow visualization results (Fig. 4(b)). These similarities imply that the three-dimensional flow structure in the cavity and around the jet can be reproduced well by the present computation.

The mass fraction of the injectant is obtained at each computational cell as a solution of the governing equations. This is why the injectant number-density can be calculated from the mass fraction and density in the cell using the molecular weight of the injectant and Avogadro's constant. Figure 6 shows the map of the computed injectant number-density on the *x*-*z* plane at *y* = 0. The number density values in the map are normalized by the value immediately above the injection port. Handa et al. (2014)[16] applied a planar laser-induced fluorescence (PLIF) technique in order to visualize the jet issuing from the injector. Figures 7(a) and (b) show the PLIF images on the *x*–*z* plane at *y* = 0 with the rectangular cavity and the proposed device, respectively. Handa et al. used acetone molecule as luminescent molecule. According to them, the fluorescence intensity is almost proportional to the number density of the jet. The PLIF images show that the jet angle from the lower wall of the duct with the proposed device is higher than that with the rectangular cavity. The angle of the jet in Fig. 6 (computational result) is almost the same as that in the PLIF image of Fig. 7(b).

Figure 8 shows the comparison of the two jet-penetration profiles obtained from computational number density (Fig. 6) and the PLIF image (Fig. 7(b)). Here, the jet penetration is defined as the height at which the computational number density or LIF intensity decreases to 10% of the maximum value. Both heights agree reasonably well for $x/d<\sim1$. However, the computational penetration height starts to deviate from the experimental height at $x/d\sim1$ and the deviation increases with x/d.

The jet penetration is affected by the two flow behaviors. One is the three-dimensionality in the steady flow around the injector. The secondary flows around the jet changes a jet angle from the lower wall of the duct; i.e., the secondary flows change the jet penetration. The other is the jet unsteadiness. In general, the jet shear-layer is unstable. The vortical structure appears owing to the instability of the shear layer and the vortical structure grows with *x*. As a result, the shear layer becomes thick with *x*. This shear layer thickening contributes to the jet penetration; i.e., the jet unsteadiness contributes to change in the jet penetration. The deviation of the computational results from the experimental results might be due to the jet unsteadiness in the actual flow because the deviation increases with *x* in Fig. 8 (the computational result corresponds to the steady state solution). The well agreement in the computational and experimental jet-penetrations near the injector ($x/d<\sim1$) implies that the three-dimensional flow

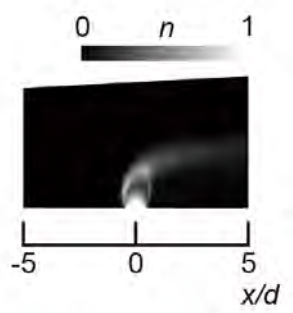

Fig. 6: Number density map.

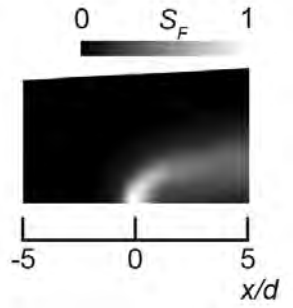

(a) duct with a rectangular cavity

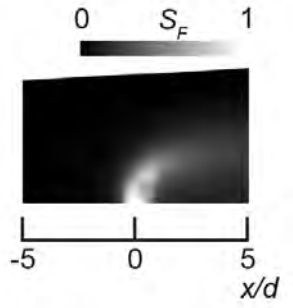

(b) duct with a three-dimensional cavity

Fig. 7: PLIF images[16].

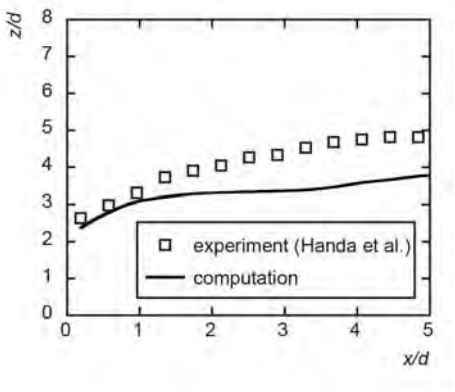

Fig. 8: Jet penetration profiles.

can be reproduced by the present computation.

The downstream end of the cut out part of the three-dimensional cavity is located at x/d=−1.33. This location is enough close to the jet. This is because the flows created by the cavity act effectively on the jet; i.e., the secondary flows move around the jet, which is one of the reasons why the jet angle from the lower wall of the duct with the proposed device becomes higher than that with the rectangular cavity. The computational jet penetration agrees with the experimental profile because the secondary flow around the jet can be reproduced well by the present computation.

The above-mentioned comparisons of the computational results with the experimental results imply that the three-dimensional flow structure can be reproduced not only inside the cavity but also around the jet by the present computation although the flow unsteadiness cannot be captured (the features related to flow unsteadiness are remarkable in the region of x/d>~1). That is to say, the present computational results are verified in the limited regions; i.e., inside the cavity and around the jet (x/d<~1). Using the verified computational results, we discuss the detailed three-dimensional structure of the flow in the following

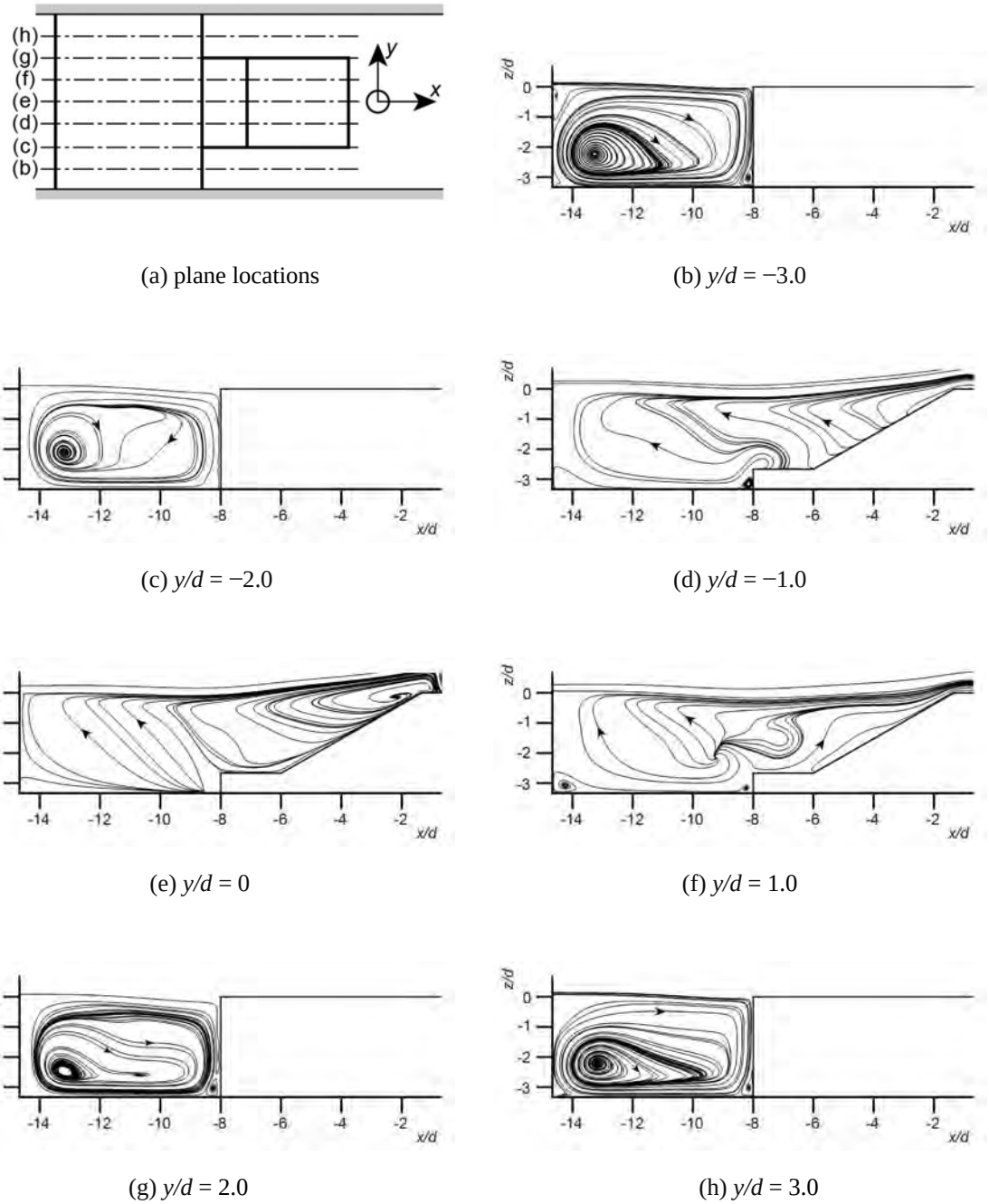

(a) plane locations

(b) y/d = −3.0

(c) y/d = −2.0

(d) y/d = −1.0

(e) y/d = 0

(f) y/d = 1.0

(g) y/d = 2.0

(h) y/d = 3.0

Fig. 9: Streamlines on the x-z plane.

paragraphs.

Figure 9 shows the streamlines in the cavity on representative *x*-*z* planes. The location of each plane is shown in Fig. 9(a). A vortex is seen near the corner between the front face and bottom wall of the cavity on the planes of *y*/*d* = −3.0, −2.0, 2.0, and 3.0 where the

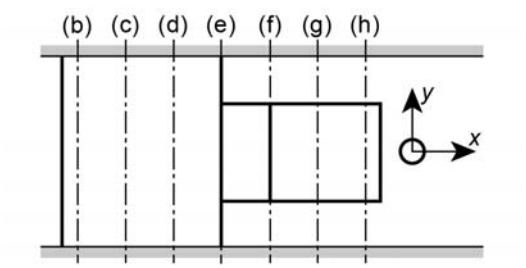

(a) plane locations

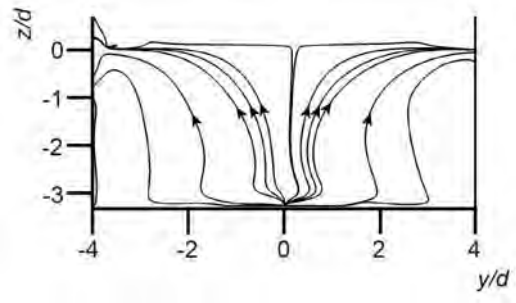

(b) *x*/*d* = −14.0

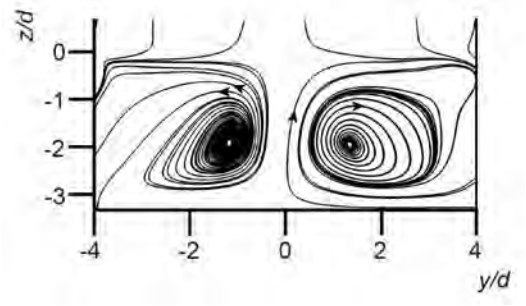

(c) *x*/*d* = −12.0

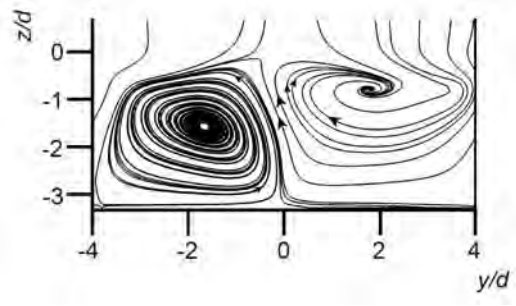

(d) *x*/*d* = −10.0

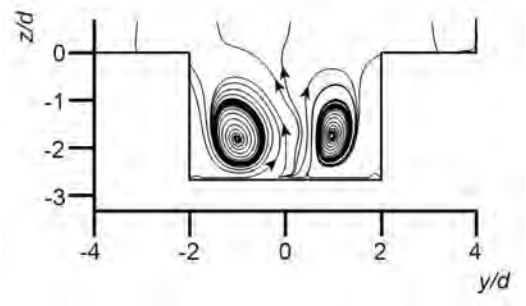

(e) *x*/*d* = −8.0

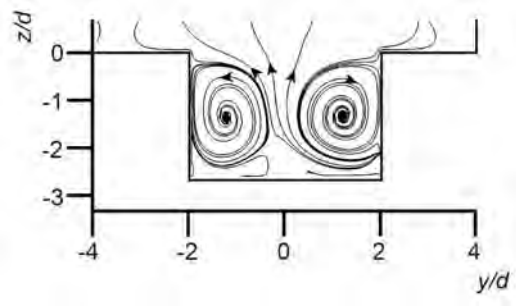

(f) *x*/*d* = −6.0

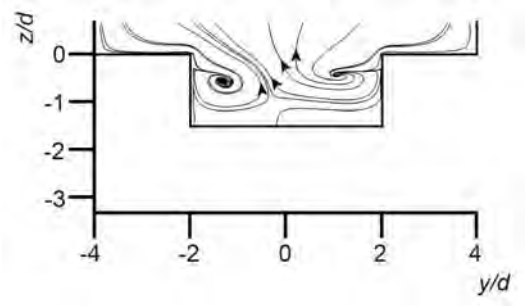

(g) *x*/*d* = −4.0

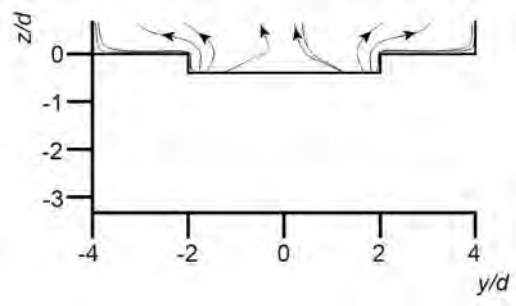

(h) *x*/*d* = −2.0

Fig. 10: Streamlines on the *y*-*z* plane.

cavity rear face is not cut out. This vortex results from the deflection of the primary flow along the cavity rear face. On the other hand, there is no remarkable vortex in the rectangular part of the cavity on the planes of y/d = −1.0, 0, and 1.0 where the cavity rear face are cut out. However, a vortex is observed near the corner between the inclined wall of the cavity and the lower wall of the duct ($x/d \sim -2.0$) on the plane of $y = 0$ (Fig. 9(e)).

Figure 10 shows the streamlines in the cavity on representative y-z planes. The location of each plane is shown in Fig. 10(a). The counter-rotating vortices are seen inside the cavity in the range of $-12.0 < x/d < -4.0$. This implies that the streamwise vortices exist in this range.

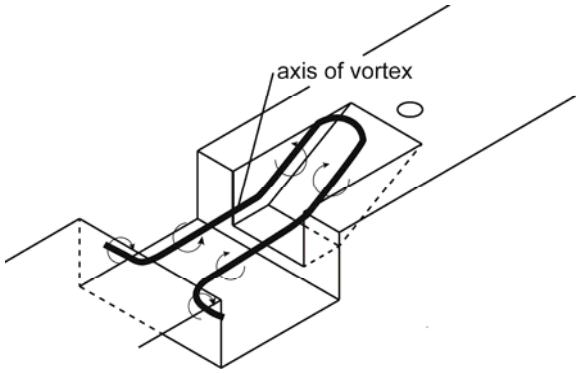

Fig. 11: Schematic diagram of vortical structure.

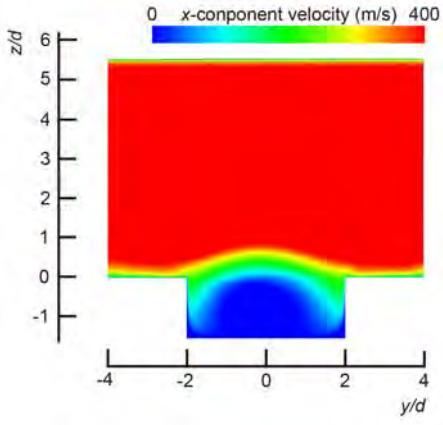

Fig. 12: Map of x-component velocity on the y-z plane ($x/d = -4.0$).

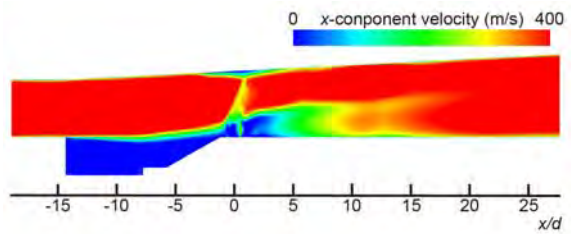

Fig. 13: Map of x-component velocity on the x-z plane ($y = 0$).

As shown in Fig. 11, the vortical structure is constructed by carefully observing the results shown in Figs. 9 and 10. The vortex placed near the corner between the front face and bottom wall of the cavity is bended to the streamwise direction. This is why the counter rotating vortices are seen on each y-z plane in Fig. 10. The vortex is bended again near the corner between the inclined wall of the cavity and the lower wall of the duct. As a result, a vortex having a three-dimensional configuration is formed in the cavity.

Figures 12 and 13 show the maps of x-component velocity on the y-z plane of $x/d = -4.0$ and on the x-z plane of $y = 0$, respectively. The flow having an upward velocity component is produced near the duct center (y = 0) owing to the counter-rotating vortices in the cut out region as shown in Figs. 10(e)−(g). This upward flow lifts up the shear layer spanning the cavity; i.e., the shear layer has a convex shape on the y-z plane as shown in Fig. 12 and the shear layer is deflected upward on the y-z plane of $y = 0$ as shown in Fig. 13. As a result, the stagnating gas under the shear layer protects the jet from the primary flow having large momentum. This is why the jet penetrates highly into the primary flow. It is expected that the slower the gas becomes in front of the jet, the more rapidly the gas flows into the region behind the jet. As a result, a large amount of mass is added behind the jet. This is also why the jet penetrates highly into the primary flow.

5. Conclusions

The supersonic mixing field induced by a novel wall-mounted cavity having a three-dimensional shape was investigated computationally by solving the Reynolds-averaged Navier-Stokes (RANS) equations. In the computation, the steady state solution was obtained. The computational results were compared with the previous experimental results of the oil-flow surface visualization and PLIF visualization. The pattern of the computed limiting streamlines agreed well with the oil-flow pattern and the computed jet-penetration height agreed with the experimental jet-penetration height near the injector; i.e., the computational results were verified by the experimental results.

The computational results revealed that a vortex having a three-dimensional shape was produced in the cavity and that the vortex in the cavity acted on the shear-layer spanning across the cavity so that it deflected upward near the central plane of the duct. It was found that owing to the shear layer deflection the jet was protected from the primary flow having large momentum. This is the primary reason why the jet penetrates highly into the primary flow.

Acknowledgment

This research used computational resources of the

PRIMERGY RX300 S7 provided by Research Institute for Information Technology of Kyushu University.

References

1) J. M. Seiner, S. M. Dash and D. C. Kenzakowski, *Journal of Propulsion and Power*, **17**, 1273 (2001).
2) M. K. Barai and B. B. Saha, *Evergreen*, **2**, 49 (2015).
3) K. Moroga, A. Nagata, Y. Kuriyama, T. Kobayashi and K. Hasegawa, *Evergreen*, **2**, 14 (2015).
4) R. C. Rogers, D. P. Capriotti and R. W. Guy, 2*0th AIAA Advanced Measurement and Ground Testing Technology Conference*, AIAA 98-2590, Albuquerque (1998).
5) P. Gerlinger, P. Sroll, M. Kindler, F. Schneider and M. Aigner, *Aerospace Science and Technology*, **12**, 159 (2008).
6) M. Vishwakarma and A. Vaidyanathan, *Acta Astronautica*, **118**, 21 (2016).
7) M. R. Gruber, A. S. Nejad, T. H. Chen, and J.C., Dutton, *Experiments in Fluids*, **22**, 397 (1997).
8) R. Srinivasan and R. D. W. Bowersox, *AIAA Journal*, **46**, 1944 (2008).
9) C. Wang, Z. Jiang, Z. Hu, and J. Lu, *Acta Mechanica Sinica*, **25**, 37 (2009)
10) P. J. Lu and K. C. Wu, *Physics of Fluids*, **3**, 3046 (1991).
11) C. Aguilera and K. H. Yu, *Journal of Propulsion and Power*, **31**, 1532 (2015).
12) K. H. Yu and K. C. Schadow, *Combustion and Flame*, **99**, 295 (1994).
13) V. Nenmeni and K. Yu, *40th AIAA Aerospace Sciences Meeting & Exhibit*, AIAA 2002-1010, Reno (2002).
14) N. Sato, A. Imamura, S. Shiba, S. Takahashi, M. Tsue and M. Kono, *Journal of Propulsion and Power*, **15**, 358 (1999).
15) A. D. Cutler, G. C. Harding, and G. S. Diskin, *AIAA Journal*, **51**, 809 (2013).
16) T. Handa, A. Nakano, K. Tanigawa, and J. Fujita, *Experiments in Fluids*, **55**, 1711 (2014).
17) F. R. Menter, *AIAA Journal*, **32**, 1598 (1994).
18) M. S. Liou, *Journal of Computational Physics*, **129**, 364 (1996).
19) D. Papamoschou, D. G. Hubbard, *Experiments in Fluids*, **14**, 468 (1993).
20) M. R. Gruber, A. S. Nejad, T. H. Chen and J. C. Dutton, *AIAA Journal*, **34**, 2191 (1996).